Efficient exciton generation in a semiconductor quantum-dot–metal-nanoparticle composite structure using conventional chirped pulses

Dionisis Stefanatos ⬤,[*] Athanasios Smponias ⬤, Ioannis Thanopulos ⬤, and Emmanuel Paspalakis ⬤
Materials Science Department, School of Natural Sciences, University of Patras, Patras 26504, Greece

We consider a nanostructure consisting of a semiconductor quantum dot coupled to a metal nanoparticle, and we show with numerical simulations that the exciton state of the quantum dot can be robustly generated from the ground state even for small interparticle distances, using conventional chirped pulses with a Gaussian envelope. The asymmetry observed in the final exciton population with respect to the chirp sign of the applied pulses is explained using the nonlinear density matrix equations describing the system and is attributed to the real part of the parameter emerging from the interaction between excitons in the quantum dot and plasmons in the metal nanoparticle. The simplicity of Gaussian chirped pulses, which can also be easily implemented in the laboratory, makes the proposed robust quantum control scheme potentially useful for the implementation of ultrafast nanoswitches and quantum information processing tasks with semiconductor quantum dots.

I. INTRODUCTION

An intense field of research is devoted to studies regarding the optical properties of complex systems composed of plasmonic nanostructures coupled to quantum entities like molecules or semiconductor quantum dots (SQDs) [1]. When the quantum part of these composite nanosystems is coherently controlled, they behave as active nanophotonic structures and are expected to have important applications in many fields, including nanotechnology and modern quantum technologies. For example, it has been found that a composite structure which consists of a SQD and a metal nanoparticle (MNP) is more efficient than a quantum dot alone for optical phenomena like the creation of single photons on demand [2,3] and polarization-entangled photons [4]. The coupled SQD-MNP nanostructure serves also as the basic system for the plasmonic nanolaser (spaser) [5,6]. In order to exploit the advantages offered by the coupled SQD-MNP system for these important quantum technology applications, a crucial problem is the efficient controlled population transfer from the ground state to the exciton state of the quantum dot, in the presence of the nanoparticle. This important problem has been explored in a series of studies [7–18], with emphasis put on the effect of the interparticle distance.

More precisely, by studying a nanostructure containing a CdTe SQD and a rodlike Au MNP, it was discovered that the period of Rabi oscillations exhibited by the exciton population is modified with the interparticle distance [7], an effect that was later associated with the development of plasmonic metaresonances [8,9]. Moreover, this last phenomenon was linked to optical bistability that may take place in a SQD-MNP nanosystem [10–12,19]. It was also shown that properly tailored pulses with a hyperbolic secant envelope can achieve high fidelity exciton state preparation in a SQD coupled to a spherical MNP [14]. The application of ultrashort pulse trains or amplitude-modulated laser pulses to the same system results in distance-dependent modulation of the exciton population in the SQD, a phenomenon which can be exploited for the implementation of efficient nanoswitches [15,16]. In another study considering a three-level V-type SQD, the MNP was exploited in order to obtain selective population transfer to one of the exciton states by applying resonant fields [13]. In a related work, optimal control was used for the effective transfer of population between the two lower states of a Λ-type SQD placed close to a spherical MNP [18].

In the majority of the previously discussed works, resonant methods have been employed for the preparation of the SQD exciton state in the presence of a MNP. The main advantage of these methods is the fast, and with high fidelity, population transfer to the exciton state, something which occurs only when using finely tuned pulse amplitudes and widths. The efficiency of resonant methods is rather sensitive to changes in the characteristics of the applied fields. A way to overcome these drawbacks and obtain robust population inversion in a two-level system is to use adiabatic methods [20,21] or the closely related shortcuts to adiabaticity [22], where the latter are essentially accelerated versions of the former, while both are implemented using chirped pulses. In our recent work we used the shortcut method of transitionless quantum driving and showed that efficient preparation of the exciton state in the SQD-MNP system can be accomplished [23].

In the current article we use conventional chirped pulses with Gaussian envelopes and linear chirp, and we demonstrate that they also can robustly prepare the exciton state in a SQD coupled to a MNP. The reason for considering such pulses is their simplicity and easiness to implement in the laboratory, compared to the more sophisticated chirp and envelopes needed by the shortcut pulses. Note that these type of pulses have been used for the efficient preparation of the

_____
[*]dionisis@post.harvard.edu

exciton [24–31] and biexciton [32–35] states in a SQD in the absence of a MNP. In the present study involving the coupled SQD-MNP system and for the employed chirped pulses we observe an asymmetry in the final exciton population, which depends on the sign of the chirp parameter, positive or negative. In the nonlinear density matrix equations describing the coupled SQD-MNP system [7–12,14–17,36–46], we explicitly identify the symmetry-breaking term as the real part of the nonlinearity self-interaction parameter, where the latter is due to the dipolar exciton-plasmon interaction [36,37]. Using the familiar two-level system terminology, this term corresponds to an effective "longitudinal" field which breaks the z symmetry in the Bloch sphere, affecting differently the "longitudinal" field associated with positive- and negative-chirp parameters.

The present work has the following structure. In Sec. II we provide the nonlinear density matrix equations which describe the interaction of the SQD-MNP system with the applied electromagnetic field. In Sec. III we describe the applied chirped pulses and also discuss the symmetry breaking in the equations for opposite-sign chirp parameters. In Sec. IV we provide numerically obtained fidelity diagrams of the exciton state final population, for various pulse durations and SQD-MNP distances. Section V summarizes the results of our research.

II. COUPLED SEMICONDUCTOR QUANTUM-DOT–METAL -NANOPARTICLE MODEL

The system under consideration is displayed in Fig. 1 and consists of a classical spherical MNP with radius α and dielectric function $\varepsilon_m(\omega)$, and a SQD with dielectric constant ε_s which is modeled as a two-level system, with states $|0\rangle$ and $|1\rangle$ corresponding to the ground and single-exciton states, respectively, an approximation used in several previous works [7–12,14–17,36–46]. The two components of the nanosystem are embedded in an environment with the dielectric constant ε_{env}, with their centers separated by a distance R.

A linearly polarized external electric field, $\vec{\mathcal{E}}(t) = \hat{z}\mathcal{E}_0 f(t)\cos[\omega t + \phi(t)]$, is applied to the nanostructure, where $\mathcal{E}_0$ is the electric field amplitude, $f(t)$ is the dimensionless pulse envelope, ω is the angular frequency, and $\phi(t)$ is the time-dependent phase. Using the methodology of the density matrix, we find the following set of equations for the population difference between the ground and the single-exciton states, $\Delta(t) = \rho_{00}(t) - \rho_{11}(t)$, and the slowly varying off-diagonal matrix element $\sigma(t) = \rho_{10}(t)e^{i[\omega t + \phi(t)]}$ [14,23,36,37,47]:

$$\dot{\Delta}(t) = i\Omega^*(t)\sigma(t) - i\Omega(t)\sigma^*(t) + 4G_I\sigma(t)\sigma^*(t)$$
$$- \frac{\Delta(t) - 1}{T_1}, \tag{1a}$$

$$\dot{\sigma}(t) = i(\delta + \dot{\phi}(t))\sigma(t) + i\frac{\Omega(t)}{2}\Delta(t) + iG\Delta(t)\sigma(t)$$
$$- \frac{\sigma(t)}{T_2}, \tag{1b}$$

where $\delta = \omega - \omega_0$ is the detuning of the applied field, with $\hbar\omega_0$ being the exciton state energy, while T_1 and T_2 denote the
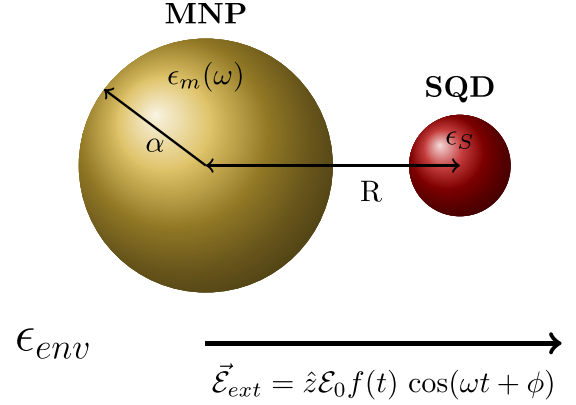

FIG. 1. Spherical metal nanoparticle with radius α and dielectric constant $\varepsilon_m(\omega)$ coupled to a semiconductor quantum dot with radius $b \ll \alpha$ and dielectric constant ε_s. R denotes the interparticle distance, ε_{env} denotes the dielectric constant of the surrounding, and $\vec{\mathcal{E}}(t)$ denotes the externally applied field.

relaxation times corresponding to spontaneous emission and dephasing in the SQD, respectively. Also, $\Omega(t)$ denotes the time-dependent complex Rabi frequency given by [36,37,47]

$$\Omega(t) = \Omega_0 f(t), \quad \Omega_0 = \frac{\mu\mathcal{E}_0}{\hbar\varepsilon_{\text{eff}S}}\left(1 + \frac{s_a\gamma_1\alpha^3}{R^3}\right), \tag{2}$$

while G is the self-interaction parameter defined as [37]

$$G = \sum_{n=1}^{N} \frac{1}{4\pi\varepsilon_{\text{env}}}\frac{(n+1)^2\gamma_n\alpha^{2n+1}\mu^2}{\hbar\varepsilon_{\text{eff}S}^2 R^{2n+4}}. \tag{3}$$

In the above formulas, μ is the dipole moment for the ground to exciton transition in the SQD, which without loss of generality is assumed to be real. Also, the quantity $\varepsilon_{\text{eff}S} = \frac{2\varepsilon_{\text{env}} + \varepsilon_S}{3\varepsilon_{\text{env}}}$ represents the SQD effective dielectric constant; $\gamma_n = \frac{\varepsilon_m(\omega) - \varepsilon_{\text{env}}}{\varepsilon_m(\omega) + (n+1)\varepsilon_{\text{env}}/n}$, with $n = 1, 2, 3, \ldots$; and $s_a = 2$ since the external field is parallel to the center line of the system (z axis). In addition, G_I is the imaginary part of $G = G_R + iG_I$. Observe that nonlinear terms arise in the above equations due to the parameter G. At $t = 0$ the initial conditions starting from the ground state are $\Delta(0) = 1$ and $\sigma(0) = 0$, while complete exciton preparation at the final time $t = t_f$ corresponds to the target value $\Delta(t_f) = -1$. The quantity that we are interested in is the final exciton population $\rho_{11}(t_f) = [1 - \Delta(t_f)]/2$.

The two parts of the complex Rabi amplitude correspond to the applied field and the field induced by the polarization of the MNP (caused also by the external field). If we write $\Omega_0 = |\Omega_0|e^{i\beta}$, where β is the corresponding phase, then the complex Rabi frequency can be expressed as $\Omega(t) = |\Omega(t)|e^{i\beta}$, where $|\Omega(t)| = |\Omega_0|f(t)$, a relation which we use in the following section. The self-interaction parameter G emerges from the interaction between SQD excitons and MNP plasmons [7,36,37]. Particularly, the external field induces a dipole on the SQD, proportional to the off-diagonal elements of the density matrix, which also induces a dipole on the MNP, which subsequently interacts with the SQD dipole [36,47]. In Eq. (3) we actually consider that the SQD dipole induces multipole moments on the MNP [37,48], and we use the
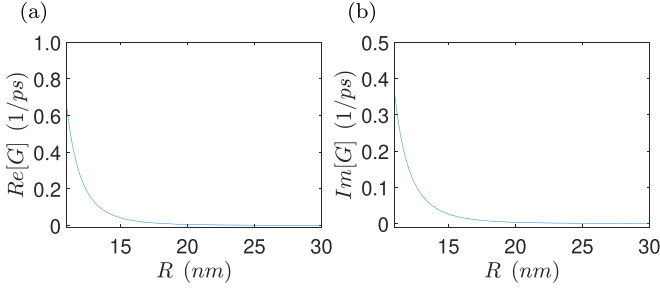
FIG. 2. Real (a) and imaginary (b) parts of the nonlinear self-interaction parameter G, as a function of the interparticle distance.

value $N = 20$ in the subsequent calculations in order to get converging results. In Fig. 2 we display the real and imaginary parts of G as a function of the interparticle distance, for the parameter values later used in Sec. IV.

III. CONVENTIONAL CHIRPED PULSES AND SYMMETRY BREAKING

In this section we explain how chirped pulses can be used for the efficient preparation of the exciton state, as well as why opposite-sign chirp parameters lead to different final fidelities, due to the symmetry breaking of the system caused by the presence of the MNP. Observe that for $G = 0$ and $T_1, T_2 \to \infty$, Eqs. (1) reduce to the Bloch equations for the two-level system:

$$i\begin{pmatrix} \dot{a}_1(t) \\ \dot{a}_2(t) \end{pmatrix} = \frac{1}{2}\begin{pmatrix} -\dot{\phi}(t) & \Omega(t) \\ \Omega^*(t) & \dot{\phi}(t) \end{pmatrix}\begin{pmatrix} a_1(t) \\ a_2(t) \end{pmatrix}, \quad (4)$$

with the mapping $\Delta(t) = |a_1(t)|^2 - |a_2(t)|^2$ and $\sigma(t) = a_1(t)a_2^*(t)$. The exciton state preparation from $\Delta(0) = 1$ to $\Delta(t_f) = -1$ corresponds to inverting the population in this two-level system. The instantaneous eigenstates of the two-level system and the corresponding eigenvalues are

$$|\psi_+(t)\rangle = \begin{pmatrix} \cos\frac{\theta(t)}{2} \\ \sin\frac{\theta(t)}{2}e^{-i\beta} \end{pmatrix}, \quad (5a)$$

$$|\psi_-(t)\rangle = \begin{pmatrix} \sin\frac{\theta(t)}{2} \\ -\cos\frac{\theta(t)}{2}e^{-i\beta} \end{pmatrix}, \quad (5b)$$

and

$$A_\pm(t) = \pm\frac{1}{2}\sqrt{\dot{\phi}^2(t) + |\Omega(t)|^2}, \quad (6)$$

where

$$\tan\theta(t) = \frac{|\Omega(t)|}{-\dot{\phi}(t)}. \quad (7)$$

If the applied electric field is selected such that the mixing angle is slowly varied from $\theta(0) = 0$ to $\theta(t_f) = \pi$, then the population inversion takes place adiabatically along the eigenstate $|\psi_+(t)\rangle$. If $\theta(0) = \pi$ is slowly modified to $\theta(t_f) = 0$, then the inversion occurs along the eigenstate $|\psi_-(t)\rangle$.

In order to achieve the desired population inversion, and thus the exciton state preparation, we use linearly chirped

Gaussian pulses

$$\mathcal{E}(t) = \frac{\hbar\epsilon_{\text{eff}S}}{\mu}\frac{\Theta}{\sqrt{2\pi\tau_0 t_p}}\exp\left[-\frac{(t-t_0)^2}{2t_p^2}\right]\cos[\omega t + \phi(t)], \quad (8)$$

which are obtained after passing a constant frequency Gaussian pulse with area Θ and initial duration τ_0 through a chirp filter with a chirp constant a [26,49]. The pulse duration is modified from τ_0 to [26,50]

$$t_p = \sqrt{\tau_0^2 + \frac{a^2}{\tau_0^2}}, \quad (9)$$

while its frequency acquires a linear chirp,

$$\dot{\phi}(t) = c(t - t_0), \quad (10)$$

with rate [26,50]

$$c = \frac{a}{a^2 + \tau_0^4}. \quad (11)$$

The final time of the pulse is taken to be $t_f = 2t_0$, where t_0 is large enough and defines the pulse center.

Observe that for $c > 0$ ($a > 0$) the mixing angle changes from 0 to π for both types of pulses, and thus the system evolves along $|\psi_+(t)\rangle$, while for $c < 0$ ($a < 0$) it changes from π to 0 and the system evolves along $|\psi_-(t)\rangle$. For $G = 0$ the two paths are equivalent but the presence of $G = G_R + iG_I$ with $G_R \neq 0$ breaks this symmetry, as we immediately show. Let $\Delta(t)$ and $\sigma(t)$ be the solution of system (1), with $\delta = 0$ and ignoring relaxation:

$$\dot{\Delta}(t) = i\Omega^*(t)\sigma(t) - i\Omega(t)\sigma^*(t) + 4G_I\sigma(t)\sigma^*(t), \quad (12a)$$

$$\dot{\sigma}(t) = i\dot{\phi}(t)\sigma(t) + i\frac{\Omega(t)}{2}\Delta(t) + iG\Delta(t)\sigma(t), \quad (12b)$$

when starting from $\Delta(0) = 1$ and $\sigma(0) = 0$ and with the chirp $\dot{\phi}$ given by Eq. (10). Let also $\Delta'(t)$ and $\sigma'(t)$ be the solution when starting from the same initial conditions $\Delta'(0) = 1$ and $\sigma'(0) = 0$, but with the opposite-sign chirp $\dot{\phi}' = -\dot{\phi}$, i.e., when using $-c$ (or $-a$) in Eq. (10). The primed variables satisfy the equations

$$\dot{\Delta}'(t) = i\Omega^*(t)\sigma'(t) - i\Omega(t)\sigma'^*(t) + 4G_I\sigma'(t)\sigma'^*(t), \quad (13a)$$

$$\dot{\sigma}'(t) = -i\dot{\phi}(t)\sigma'(t) + i\frac{\Omega(t)}{2}\Delta'(t) + iG\Delta'(t)\sigma'(t), \quad (13b)$$

where we observe that the difference with system (12) is that $\dot{\phi}$ is replaced by $-\dot{\phi}$. Now let us consider the following transformation:

$$\Delta''(t) = \Delta'(t), \quad (14a)$$

$$\sigma''(t) = -\sigma'^*(t)e^{2i\beta}. \quad (14b)$$

It is not hard to show that the transformed variables satisfy the equations

$$\dot{\Delta}''(t) = i\Omega^*(t)\sigma''(t) - i\Omega(t)\sigma''^*(t) + 4G_I\sigma''(t)\sigma''^*(t), \quad (15a)$$

$$\dot{\sigma}''(t) = i\dot{\phi}(t)\sigma''(t) + i\frac{\Omega(t)}{2}\Delta''(t) - iG^*\Delta''(t)\sigma''(t). \quad (15b)$$

Observe that in Eqs. (15) the chirp sign has been restored $(+\dot{\phi})$, and the only difference with Eqs. (12) is that G is replaced by $-G^* = -G_R + iG_I$. For $G_R = 0$, Eqs. (12) and (15) are identical, and since the transformed variables satisfy also the same initial conditions $\Delta''(0) = 1$, $\sigma''(0) = 0$, we obtain that $\Delta''(t) = \Delta(t)$. But also $\Delta'(t) = \Delta''(t)$, and thus $\Delta'(t) = \Delta(t)$ and the solutions corresponding to the opposite-sign chirp are equivalent. For $G_R \neq 0$ this symmetry breaks down. Note also that mathematically the symmetry is preserved if G is replaced by $G' = -G^*$.

There is actually a simple intuitive explanation why the presence of G_R breaks the "z symmetry" of the two-level system (Bloch sphere), which is revealed when we rewrite Eq. (12b) for the coherence as

$$\dot{\sigma}(t) = i[\dot{\phi}(t) + G_R\Delta(t)]\sigma(t) + i\frac{\Omega(t)}{2}\Delta(t) - G_I\Delta(t)\sigma(t),$$
(16)

using that $G = G_R + iG_I$. Now it is obvious that $G_R \neq 0$ results in an extra time-dependent field $G_R\Delta(t)$ in the "z direction," defined with respect to the two-level system (4), which breaks the corresponding symmetry for positive- and negative-chirp $\dot{\phi}(t)$. In the two-level Schrodinger equation (4) the $\dot{\phi}(t)$ term should be replaced by $\dot{\phi}(t) + G_R\Delta(t)$ and the instantaneous "eigenvalues" (6) become state dependent:

$$A_\pm(t) = \pm\frac{1}{2}\sqrt{[\dot{\phi}(t) + G_R\Delta(t)]^2 + |\Omega(t)|^2},$$
(17)

where for the latter term we use quotation marks since in the presence of the MNP the system is nonlinear. In the next section we present specific examples of how the added term $G_R\Delta(t)$ modifies the gap between the "eigenvalues" for the different chirp signs. Note that in Eq. (4), the term $\dot{\phi}(t)$ multiplies the $-\sigma_z$ Pauli spin matrix while the term $\Omega(t)$ multiplies a linear combination of the σ_x and σ_y matrices, and this is why we characterize them as the "longitudinal" and "transverse" fields, respectively. Nevertheless, we point out that the "transverse" field $\Omega(t)$ for the two-level system corresponds to the applied field, which points in the z direction in the real space.

IV. NUMERICAL SIMULATIONS AND RESULTS ANALYSIS

Here, we test the performance of the previously discussed chirped pulses with numerical simulations of the system in Eqs. (1), including the effect of nanoparticle as well as relaxation. For the parameters that appear in these equations and are necessary in the simulations, we use numerical values typically corresponding to CdSe-based SQD, which have also been used in many other works regarding similar systems: $T_1 = 0.8$ ns, $T_2 = 0.3$ ns, $\varepsilon_{env} = \varepsilon_0$, $\varepsilon_s = 6\varepsilon_0$, $\hbar\omega_0 = 2.5$ eV, $\mu = 0.65$ e nm, and $\alpha = 7.5$ nm, where as usual ε_0 denotes the vacuum dielectric constant. For $\varepsilon_m(\omega)$, we use the experimental value corresponding to gold [51], which is specifically $\varepsilon_m(\omega) = -2.278\,29 + i3.812\,64$.

In Fig. 3 we display contour plots of the final exciton population $\rho_{11}(t_f)$ versus the pulse area and chirp, when applying the chirped Gaussian pulse (8) with $\tau_0 = 1$ ps to the SQD-MNP system, for several interparticle distances. Observe that for the smallest distance $R = 11$ nm [Fig. 3(a)],
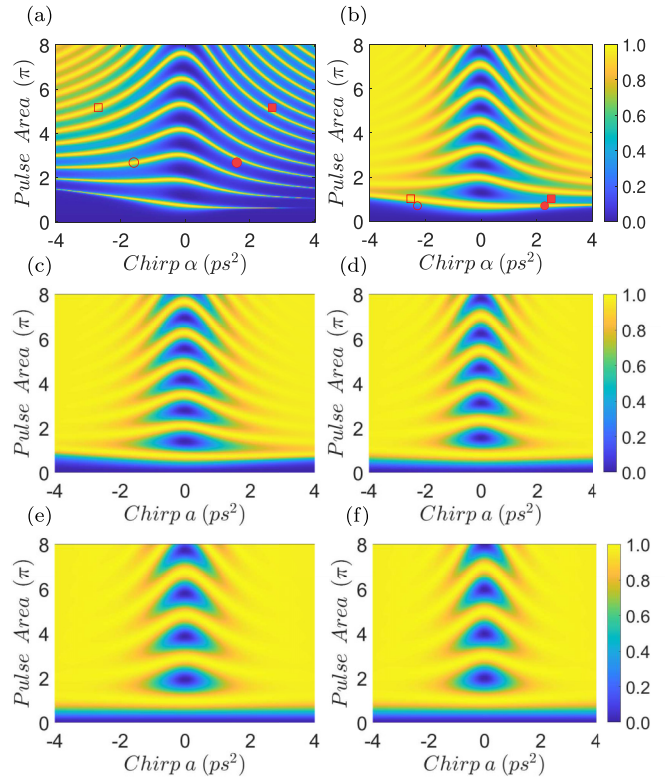

FIG. 3. Contour plot of the final exciton population when using the Gaussian chirped pulse with $\tau_0 = 1$ ps, versus the pulse area and the chirp parameter a, for different values of the interparticle distance: (a) $R = 11$ nm, (b) $R = 12$ nm, (c) $R = 13$ nm, (d) $R = 15$ nm, (e) $R = 30$ nm, and (f) $R = 80$ nm.

efficient population transfer is achieved only at some narrow strips corresponding to specific combinations of pulse area and chirp, resembling the performance of resonant pulses. The reason is that for such small distances the nonlinear term G is very strong and practically destroys the adiabatic following and cancels the beneficial effect of the chirp. The situation is drastically improved for a small change in the interparticle distance [see Fig. 3(b) corresponding to $R = 12$ nm]. Due to the reduction of G, now the high-fidelity stripes become wider and occupy a larger portion of the contour diagram. For distances as small as 13 and 15 nm [see Figs. 3(c) and 3(d), respectively], robust population transfer is accomplished for sufficiently large absolute chirp values and pulse areas larger than a chirp-dependent lower threshold. For larger distances, where the effect of the MNP weakens, the contour diagrams become almost independent of R [see, for example, Figs. 3(e) and 3(f) corresponding to $R = 30$ nm and $R = 80$ nm, which look identical]. Figure 4 is obtained similarly to Fig. 3 by applying a linearly chirped Gaussian pulse with shorter $\tau_0 = 0.75$ ps. Obviously, the overall performance and robustness are now improved. This can be understood by using the analysis of the previous section. Specifically, from Eq. (11) we see that, for fixed a, the chirp rate c is larger for smaller τ_0. Accordingly, the initial and final chirp values, $|\dot{\phi}(0)| = |\dot{\phi}(2t_0)| = |c|t_0$, are larger for smaller τ_0. But from the discussion at the end of the previous section, we know that the unwanted term affecting the dynamics has the form
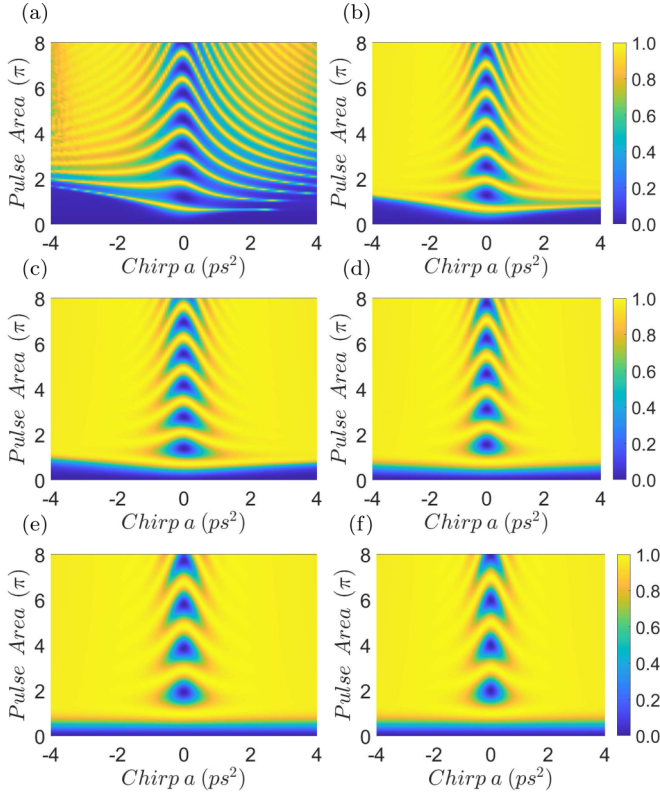
FIG. 4. Contour plot of the final exciton population when using the Gaussian chirped pulse with $\tau_0 = 0.75$ ps, versus the pulse area and the chirp parameter a, for different values of the interparticle distance: (a) $R = 11$ nm, (b) $R = 12$ nm, (c) $R = 13$ nm, (d) $R = 15$ nm, (e) $R = 30$ nm, and (f) $R = 80$ nm.

$G_R \Delta(t)$, and thus it is stronger at the beginning and at the end, where $|\Delta|$ is close to unity. The larger chirp for smaller τ_0 during the same time intervals cancels more effectively the undesirable action of this term.

Probably the most striking feature of Figs. 3 and 4 is the asymmetry for positive and negative chirp, evident for small values of the interparticle distance, where the symmetry-breaking term $G_R \Delta(t)$ identified in the previous section is stronger. In order to numerically confirm the previous theoretical analysis, we manually set $G_R = 0$ while keeping nonzero G_I in Eqs. (1). The results for $G_R = 0$ are displayed in Figs. 5(a) and 5(b), where we show contour plots of the final exciton population versus the pulse area and chirp, for a distance of $R = 12$ nm and a Gaussian chirped pulse with $\tau_0 = 1$ ps and $\tau_0 = 0.75$ ps, respectively. Comparing these to the corresponding figures with nonzero G_R [Figs. 3(b) and 4(b)], it becomes obvious that the asymmetry has been disappeared. We also observe that, if we manually invert the sign of G_R, the chirp asymmetry is also inverted, as shown in Figs. 5(c) and 5(d), where the same parameters as those in Figs. 3(b) and 4(b) are used. We emphasize, of course, that these manual changes in G_R are performed only for demonstration reasons, while the real values of this parameter are displayed in Fig. 2(a). Another interesting observation which can be made from Figs. 3(a) and 3(b) and Figs. 4(a) and 4(b) is that, for negative chirp, once the (larger) pulse area threshold is surpassed and for higher chirp parameter values, the
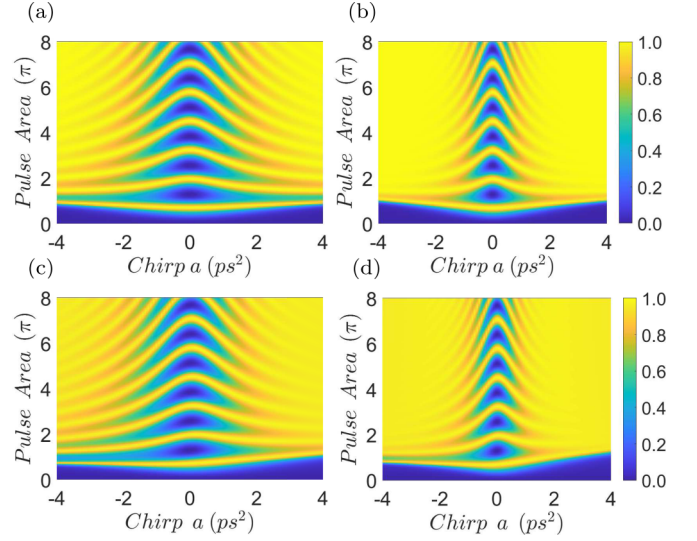

FIG. 5. Contour plot of the final exciton population versus the pulse area and the chirp parameter a for $R = 12$ nm when (a), (b) manually enforcing $G_R = \mathrm{Re}\{G\} = 0$ and (c, d) manually inverting the sign of $G_R = \mathrm{Re}\{G\}$. The initial pulse duration is taken to be $\tau_0 = 1$ ps in panels (a) and (c) and $\tau_0 = 0.75$ ps in panels (b) and (d).

population transfer is more robust compared to positive chirp. This can be explained since for negative chirp the "detuning" $\dot{\phi}(t)$ and the term $G_R \Delta(t)$ evolve in the same direction, i.e., from positive to negative values, while for positive chirp they evolve in opposite directions [recall that $G_R > 0$, see Fig. 2(a), while $\Delta(t)$ changes from its maximum value one to negative values]. This is also demonstrated in Fig. 6, where we display the modified "eigenvalues" (17) for the positive chirp (red
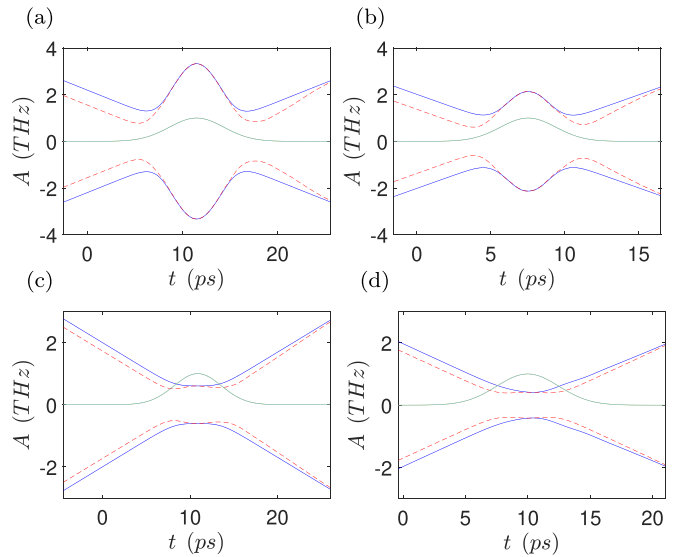

FIG. 6. Modified "eigenvalues" (17) for opposite-sign chirp values. Red dashed curves correspond to the positive chirp while blue solid curves correspond to the opposite negative chirp. The parameters used for each case correspond to (a) the upper symmetric pair marked in Fig. 3(a); (b) the lower symmetric pair marked in Fig. 3(a); (c) the upper symmetric pair marked in Fig. 3(b); and (d) the lower symmetric pair marked in Fig. 3(b).

dashed curves) and the opposite negative chirp (blue solid curves). Specifically, in Fig. 6(a) we plot the "eigenvalues" for the upper pair of opposite-sign chirp values marked in Fig. 3(a), while in Fig. 6(b) we plot the eigenvalues for the lower pair marked in Fig. 3(a). Analogously, in Figs. 6(c) and 6(d) we plot the eigenvalues for the opposite chirp pairs marked in Fig. 3(b). Observe that in all the displayed cases, the gap between the eigenvalues is larger for the negative chirp (blue solid curves) than for the positive chirp (red dashed curves). We also observe that the difference in the gap for the opposite chirp is larger for $R = 11$ nm, upper row in Fig. 6, than for $R = 12$ nm, lower row in Fig. 6, since the symmetry-breaking parameter G_R is stronger for smaller distances. By manually inverting the sign of G_R this asymmetry is also inverted, as is demonstrated in Figs. 5(c) and 5(d). At this point it is worth noting that asymmetry in the final exciton population with respect to the chirp sign has also been observed for a SQD without the presence of a MNP, where the main source of decoherence is taken to be the coupling to acoustic phonons [26,28].

In closing, we would like to point out that similar results can be obtained using chirped pulses with a hyperbolic secant envelope and a hyperbolic tangent chirp [14].

V. CONCLUSION

In this article, we showed with numerical simulations the efficient generation of the exciton state in a coupled semiconductor quantum-dot–metal-nanoparticle system, even for short interparticle distances, using linearly chirped Gaussian pulses. The asymmetry observed in the final exciton population with respect to the chirp sign of the applied pulses was also explained using the system equations. The symmetry-breaking term was identified as the real part of the nonlinearity parameter emerging from the interaction between excitons in the quantum dot and plasmons in the metal nanoparticle. This robust quantum control scheme, involving the easily implementable chirped pulses, can find application in the implementation of ultrafast nanoswitches and quantum information processing tasks with semiconductor quantum dots.

[1] B. Szychowski, M. Pelton, and M. C. Daniel, Nanophotonics **8**, 517 (2019).

[2] A. Ridolfo, O. Di Stefano, N. Fina, R. Saija, and S. Savasta, Phys. Rev. Lett. **105**, 263601 (2010).

[3] J. Straubel, R. Filter, and C. Rockstuhl, and K. Słowik, Phys. Rev. B **93**, 195412 (2016).

[4] I. S. Maksymov, A. E. Miroshnichenko, and Y. S. Kivshar, Phys. Rev. A **86**, 011801(R) (2012).

[5] M. I. Stockman, J. Opt. **12**, 024004 (2010).

[6] D. Lelwala Gamacharige, S. D. Gunapala, M. I. Stockman, and M. Premaratne, Phys. Rev. B **99**, 115405 (2019).

[7] M.-T. Cheng, S.-D. Liu, H.-J. Zhou, Z.-H. Hao, and Q.-Q. Wang, Opt. Lett. **32**, 2125 (2007).

[8] S. M. Sadeghi, Nanotechnology **20**, 225401 (2009).

[9] S. M. Sadeghi, Phys. Rev. B **79**, 233309 (2009).

[10] A. V. Malyshev and V. A. Malyshev, Phys. Rev. B **84**, 035314 (2011).

[11] B. S. Nugroho, A. A. Iskandar, V. A. Malyshev, and J. Knoester, J. Chem. Phys. **139**, 014303 (2013).

[12] F. Carreño, M. A. Antón, and E. Paspalakis, J. Appl. Phys. **124**, 113107 (2018).

[13] M. A. Antón, F. Carreño, S. Melle, O. G. Calderón, E. Cabrera-Granado, J. Cox, and M. R. Singh, Phys. Rev. B **86**, 155305 (2012).

[14] E. Paspalakis, S. Evangelou, and A. F. Terzis, Phys. Rev. B **87**, 235302 (2013).

[15] S. M. Sadeghi, Phys. Rev. B **82**, 035413 (2010).

[16] W. X. Yang, A. X. Chen, Z. Huang, and R. K. Lee, Opt. Express **23**, 13032 (2015).

[17] R. J. McMillan, L. Stella, and M. Grüning, Phys. Rev. B **94**, 125312 (2016).

[18] Y. Qi, C.-C. Shu, D.-Y. Dong, I. R. Petersen, K. Jacobs, and S.-Q. Gong, J. Phys. D: Appl. Phys. **52**, 425101 (2019).

[19] E. Paspalakis, S. Evangelou, S. G. Kosionis, and A. F. Terzis, J. Appl. Phys. **115**, 083106 (2014).

[20] N. V. Vitanov, T. Halfmann, B. W. Shore, and K. Bergmann, Annu. Rev. Phys. Chem. **52**, 763 (2001).

[21] D. Goswami, Phys. Rep. **374**, 385 (2003).

[22] D. Guéry-Odelin, A. Ruschhaupt, A. Kiely, E. Torrontegui, S. Martínez-Garaot, and J. G. Muga, Rev. Mod. Phys. **91**, 045001 (2019).

[23] A. Smponias, D. Stefanatos, and E. Paspalakis, J. Appl. Phys. **129**, 123107 (2021).

[24] Y. W. Wu, I. M. Piper, M. Ediger, P. Brereton, E. R. Schmidgall, P. R. Eastham, M. Hugues, M. Hopkinson, and R. T. Phillips, Phys. Rev. Lett. **106**, 067401 (2011).

[25] C.-M. Simon, T. Belhadj, B. Chatel, T. Amand, P. Renucci, A. Lemaitre, O. Krebs, P. A. Dalgarno, R. J. Warburton, X. Marie, and B. Urbaszek, Phys. Rev. Lett. **106**, 166801 (2011).

[26] S. Lüker, K. Gawarecki, D. E. Reiter, A. Grodecka-Grad, V. M. Axt, P. Machnikowski, and T. Kuhn, Phys. Rev. B **85**, 121302(R) (2012).

[27] Y. J. Wei, Y. M. He, M. C. Chen, Y. N. Hu, Y. He, D. Wu, C. Schneider, M. Kamp, S. Höfling, C. Y. Lu, and J.-W. Pan, Nano Lett. **14**, 6515 (2014).

[28] R. Mathew, E. Dilcher, A. Gamouras, A. Ramachandran, Hong Yi Shi Yang, S. Freisem, D. Deppe, and K. C. Hall, Phys. Rev. B **90**, 035316 (2014).

[29] T. Kaldewey, S. Lüker, A. V. Kuhlmann, S. R. Valentin, J.-M. Chauveau, A. Ludwig, A. D. Wieck, D. E. Reiter, T. Kuhn, and R. J. Warburton, Phys. Rev. B **95**, 241306(R) (2017).

[30] A. Mukherjee, A. Widhalm, D. Siebert, S. Krehs, N. Sharma, A. Thiede, D. Reuter, J. Förstner, and A. Zrenner, Appl. Phys. Lett. **116**, 251103 (2020).

[31] A. Ramachandran, J. Fraser-Leach, S. O'Neal, D. G. Deppe, and K. C. Hall, Opt. Express **29**, 41766 (2021).

[32] H. Y. Hui and R. B. Liu, Phys. Rev. B **78**, 155315 (2008).

[33] M. Glässl, A. M. Barth, K. Gawarecki, P. Machnikowski, M. D. Croitoru, S. Lüker, D. E. Reiter, T. Kuhn, and V. M. Axt, Phys. Rev. B **87**, 085303 (2013).

[34] A. Debnath, C. Meier, B. Chatel, and T. Amand, Phys. Rev. B **88**, 201305(R) (2013).

[35] T. Kaldewey, S. Lüker, A. V. Kuhlmann, S. R. Valentin, A. Ludwig, A. D. Wieck, D. E. Reiter, T. Kuhn, and R. J. Warburton, Phys. Rev. B **95**, 161302(R) (2017).

[36] W. Zhang, A. O. Govorov, and G. W. Bryant, Phys. Rev. Lett. **97**, 146804 (2006).

[37] J.-Y. Yan, W. Zhang, S.-Q. Duan, X.-G. Zhao, and A. O. Govorov, Phys. Rev. B **77**, 165301 (2008).

[38] A. Hatef, S. M. Sadeghi, and M. R. Singh, Nanotechnology **23**, 205203 (2012).

[39] J.-B. Li, N.-C. Kim, M.-T. Cheng, L. Zhou, Z.-H. Hao, and Q.-Q. Wang, Opt. Express **20**, 1856 (2012).

[40] S. G. Kosionis, A. F. Terzis, V. Yannopapas, and E. Paspalakis, J. Phys. Chem. C **116**, 23663 (2012).

[41] S. G. Kosionis, A. F. Terzis, S. M. Sadeghi, and E. Paspalakis, J. Phys.: Condens. Matter **25**, 045304 (2013).

[42] S. M. Sadeghi and C. Mao, J. Appl. Phys. **121**, 014309 (2017).

[43] A. Mohammadzadeh and M. Miri, J. Appl. Phys. **123**, 043111 (2018).

[44] S. G. Kosionis and E. Paspalakis, J. Appl. Phys. **124**, 223104 (2018).

[45] H. Hapuarachchi, S. D. Gunapala, Q. Bao, M. I. Stockman, and M. Premaratne, Phys. Rev. B **98**, 115430 (2018).

[46] S. G. Kosionis and E. Paspalakis, J. Phys. Chem. C **123**, 7308 (2019).

[47] R. D. Artuso and G. W. Bryant, Phys. Rev. B **82**, 195419 (2010).

[48] R. D. Artuso, G. W. Bryant, A. Garcia-Etxarri, and J. Aizpurua, Phys. Rev. B **83**, 235406 (2011).

[49] B. E. A. Saleh and M. C. Teich, *Fundamentals of Photonics*, 2nd ed. (Wiley Interscience, New York, 2007).

[50] V. S. Malinovsky and J. L. Krause, Eur. Phys. J. D **14**, 147 (2001).

[51] P. B. Johnson and R. W. Christy, Phys. Rev. B **6**, 4370 (1972).